Title

A sparse orthogonal collimator for small animal intensity-modulated radiation therapy part I: Planning system development and commissioning

Journal

Medical Physics, 46(12)

ISSN

0094-2405

Authors

Woods, Kaley
Nguyen, Dan
Neph, Ryan
et al.

Publication Date

2019-12-01

DOI

10.1002/mp.13872

Peer reviewed

HHS Public Access

Author manuscript

Med Phys. Author manuscript; available in PMC 2020 December 01.

Published in final edited form as:

Med Phys. 2019 December ; 46(12): 5703–5713. doi:10.1002/mp.13872.

A Sparse Orthogonal Collimator for Small Animal Intensity Modulated Radiation Therapy Part I: Planning System Development and Commissioning

Kaley Woods[1], **Dan Nguyen**[1,a], **Ryan Neph**[1], **Dan Ruan**[1], **Daniel O'Connor**[1,b], **Ke Sheng**[1]

[1]Department of Radiation Oncology, University of California Los Angeles, Los Angeles, CA

Abstract

Purpose—To achieve more translatable preclinical research results, small animal irradiation needs to more closely simulate human radiotherapy. Although the clinical gold standard is intensity modulated radiation therapy (IMRT), the direct translation of this method for small animals is impractical. In this study we describe the treatment planning system for a novel dose modulation device to address this challenge.

Methods—Using delineated target and avoidance structures, a rectangular aperture optimization (RAO) problem was formulated to penalize deviations from a desired dose distribution and limit the number of selected rectangular apertures. RAO was used to create IMRT plans with highly concave targets in the mouse brain, and the plan quality was compared to that using a hypothetical miniaturized multileaf collimator (MLC). RAO plans were also created for a realistic application of mouse whole liver irradiation and for a highly complex 2D dose distribution as a proof-of-principle. Beam commissioning data, including output and off-axis factors and percent depth dose (PDD) curves, was acquired for our small animal irradiation system and incorporated into the treatment planning system. A plan post-processing step was implemented for aperture-size-specific dose recalculation and aperture weighting reoptimization.

Results—The first RAO test case achieved highly conformal doses to concave targets in the brain, with substantially better dose gradient, conformity, and target dose homogeneity than the hypothetical miniaturized MLC plans. In the second test case, a highly conformal dose to the liver was achieved with significant sparing of the kidneys. RAO also successfully replicated a complex 2D dose distribution with three prescription dose levels. Energy spectra for field sizes 1 to 20 mm were calculated to match the measured PDD curves, with maximum and mean dose deviations of 4.47 ± 0.30% and 1.71 ± 0.18%. The final reoptimization of aperture weightings for the complex RAO test plan was able to reduce the maximum and mean dose deviations between the optimized and recalculated dose distributions from 10.3 to 6.6% and 4.0 to 2.8%, respectively.

Corresponding Author: Ke Sheng, 200 Medical Plaza, Suite B265, Los Angeles, CA 90095, 310-267-8979, KSheng@mednet.ucla.edu.

[a]Present affiliation is The University of Texas Southwestern Medical Center

[b]Present affiliation is The University of San Francisco

Conflict of Interest

The authors have no relevant conflicts of interest to disclose.

Conclusions—By using advanced optimization techniques, complex IMRT plans were achieved using a simple dose modulation device. Beam commissioning data was incorporated into the treatment planning process to more accurately predict the resulting dose distribution. This platform substantially reduces the gap in treatment plan quality between clinical and preclinical radiotherapy, potentially increasing the value and flexibility of small animal studies.

Keywords

Small animal radiotherapy; preclinical research; intensity modulated radiation therapy; collimator; direct aperture optimization

Introduction

Since over 50% of cancer patients can benefit from radiotherapy,[1–3] it is not surprising that this is a field of extensive research and constant technological advancement. As a result, improvements in radiotherapy techniques have greatly increased dose conformity and normal tissue sparing. Intensity-modulated radiation therapy (IMRT), the current clinical gold standard, allows for the delivery of extremely precise, complex dose distributions, enabling the use of escalated doses and more novel techniques such as dose painting. However, the clinical benefits gained from simply improving dose distributions will likely plateau due to normal tissue tolerances and may not improve outcomes for radioresistant tumors.[4] Highly conformal treatment is possible due to advancements in image guidance and treatment planning technology, both in terms of hardware and software, but this has been driven by physics and engineering developments rather than emergent knowledge of the underlying radiobiology of tumors and normal tissue. In order to better understand which novel treatment techniques will actually translate to improved clinical outcomes, preclinical validation is required.

Small animal models, particularly mouse models, are the most widely used tool for preclinical research, providing a low-cost, versatile way to gain valuable insight into cancer growth and radiation effects.[5–7] They also provide a practical avenue for testing the safety of new drugs and combination therapies prior to human exposure. However, the translation of these results to clinical outcomes is extremely poor.[3,8–10] A systematic review by Hackman et al[11] showed that out of 76 highly-cited animal studies only 28 were replicated in human trials, and 14 of these had outcomes contradicting the animal trials. There was even an NCI Radiation Research Program workshop held to discuss the “Lessons Learned from Radiation Oncology Clinical Trials” in which ten well-designed, randomized clinical trials from the Radiation Therapy Oncology Group were examined, with nine of these resulting in null or negative results.[12]

For these preclinical radiotherapy studies, translation is limited in large part by the irradiation techniques used. Differences in fractionation and treatment setup can drastically change the response of cancer cells to radiation.[13,14] The use of much lower energy x-rays for small animals (kilovoltage vs. megavoltage) results in different dose distributions within the tissue, as well as potential differences in relative biological effectiveness.[15–17] The use of very small field sizes can also be an issue, since both the dose rate and the dose prediction

accuracy decrease significantly.[18] Previously, preclinical studies used only crude irradiation techniques and protocols that did not account for these factors. These studies typically used radiation systems intended for human use, which are not nearly precise enough for the small animal scale. Very limited imaging was used, partially due to the inability of these human systems to achieve the resolution required for small animals. This lack of geometrical targeting necessitated the use of large radiation fields, therefore delivering high doses to normal tissue as well. Most preclinical research thus far has been done with these single large fields and very crude dose calculations, in stark contrast to the highly conformal, precisely calculated (and verified) doses delivered clinically. These dosimetric uncertainties or inaccuracies can have a major impact on the radiobiological outcomes of these studies.[19,20]

The recent development of image-guided small animal irradiators has therefore greatly expanded the potential for preclinical radiotherapy studies.[21] The two main systems are the Small Animal Radiation Research Platform (SARRP) (Xstrahl Inc., Suwanee, GA) and the X-RAD SmART (Precision X-Ray, Inc., North Branford, CT). These systems both feature cone beam CT imaging and their own dedicated treatment planning systems (Muriplan and SmART-Plan, respectively). For both irradiators, beam collimation is typically achieved using interchangeable circular or rectangular inserts ranging from 1 mm diameter to 10 × 10 cm square.[22,23]

In order for preclinical studies to accurately predict patient outcomes, the techniques employed must be analogous to those used in the clinic. IMRT relies on inverse fluence map optimization combined with dose modulating hardware, both of which must be adapted for the small animal scale in order to successfully employ this technique in preclinical studies. While the two systems mentioned above offer major improvements in preclinical radiotherapy techniques, they still lack the necessary foundations for IMRT. Clinical dose modulation is achieved with a dynamic multileaf collimator (MLC), but due to its complexity, the miniaturization of the dynamic MLC for small animals is extremely difficult and has yet to be achieved. While small animal IMRT has been attempted without an MLC by raster scanning with a 1 mm cone,[24] this technique is prohibitively slow and is subject to significant uncertainties due to improper beam modeling for small field sizes.[24] Another method has been proposed using motorized orthogonal jaws,[25] but is limited by the heuristic optimization algorithm and the relatively inefficient hardware, resulting in long treatment times, and degraded dosimetry. While there have been several other attempts to develop a miniature dose modulation device, none have proven feasible for small animal IMRT. These previous efforts are described in Part II of this report, which focuses on the hardware development and commissioning.

In this study, we introduce a new method to deliver small animal IMRT using the previously described sparse orthogonal collimator (SOC),[26] with four orthogonal leaf pairs, that can be more easily miniaturized for the small animal scale, and a planning system that supports the use of this simple dose modulation device. We demonstrate the performance of this new method on representative IMRT cases, including highly concave dose distributions and simultaneous integrated boost plans. We also detail the measurement and incorporation of

beam commissioning data into our treatment planning system and the design for the SOC hardware.

Materials and Methods

This novel small animal IMRT method is based on the idea that direct aperture optimization (DAO) can be performed using only rectangular apertures for IMRT planning. We will first introduce the optimization algorithm, then describe the beam commissioning procedure and SOC design.

Rectangular Aperture Optimization

For SOC-based IMRT we have formulated the Rectangular Aperture Optimization (RAO), which has been described in more detail previously,[26] as

$$\underset{\alpha}{\mathrm{argmin}}\ \frac{1}{2}\left\| W\left(ARx - d_0\right)\right\|_2^2 + \lambda \left\| \alpha \right\|_1 \quad \text{subject to } \alpha \geq 0. \tag{1}$$

The optimization variable, α, is a vector of coefficients. The matrix R is a scaling function which converts the coefficients of alpha to rectangular apertures in the fluence domain. Each column of R represents one rectangular aperture in the fluence domain, which configures a direct correspondence between each coefficient in alpha and a rectangular fluence of varied size and position. The matrix, A, converts the fluence to the dose domain. The desired dose, d_0, is set to the prescription dose at the PTV and zero elsewhere. The diagonal weighting matrix, W, controls the relative importance of the structures of interest. The definition of the norm with parameter p, for some vector x of dimension n, is $\| x \|_p = \sqrt[p]{\sum_{i=1}^{n} |x_i|^p}$. The L2-norm fidelity term is used to penalize deviations from d_0, and the L1-norm encourages the vector α to be sparse. The regularization weighting term, λ, is utilized to regulate the number of non-zero coefficients, and can be adjusted to meet the needs of a particular plan (i.e. to prioritize dosimetric quality or delivery efficiency). This problem formulation can be solved with a first-order primal-dual algorithm known as the Chambolle-Pock algorithm.[27–30]

The mapping, R, represents discrete rectangles in the fluence domain, and the enumeration of every rectangle quickly becomes numerically intractable for fluence maps with a large number of beamlets. Instead, we start with an over-represented set of rectangles that have side lengths of $2^n \times 2^m$, where $n, m \in \{0,1,2, \ldots, k\}$. The size of the fluence map is constrained to be $2^k \times 2^k$. Since R has a limited number of rectangles it represents, a step is added to update R with potentially important rectangles for selection. This step is performed in an alternating fashion with the optimization in equation (1). The update method first takes pairwise combinations of all the apertures that have an associated non-zero coefficient from α. A new aperture is generated from the union of the aperture shapes from each pair, and is added to R if the new aperture is rectangular and is unique to the current apertures available in R. The optimization in equation (1) and this update method are alternated until no more

new apertures are added to *R*. A detailed explanation of the initial over-represented set and the update method was previously described.[26]

RAO Evaluation

Three planning experiments were executed to validate RAO for SOC-based small animal IMRT. The aim of the first experiment was to evaluate the ability to create highly concave distributions and compare the quality of plans delivered with the SOC versus a hypothetical miniature MLC. A U-shaped target was first created on microCT images of a mouse brain (Mouse U). A more complex target volume was then created with two overlapping U and C-shaped targets (Mouse UC). Two plans were created for each target set, one with a hypothetical conventional MLC with 0.5 mm resolution and the other with the SOC. This hypothetical MLC is based on an unrealistic miniaturized system with idealized beamlets to mimic a best-case scenario, rather than a realistic system for the small animal scale. The MLC plans were created by first performing a beamlet-based fluence map optimization, regularized by anisotropic total variation, as described in a previous publication.[31] The resulting fluence maps were then segmented such that the number of deliverable apertures matched that of the SOC plan. For the Mouse U case, the U-shaped target was treated to 10 Gy. For the Mouse UC case, the non-overlapping volume was treated to 10 Gy, and the overlapped volume was treated to 12.5 Gy, a 25% dose boost.

In the second experiment, a 3D-printed mouse phantom modeled from mouse CT data was used to demonstrate a realistic application for the SOC. One preclinical research area in which the SOC could be beneficial is investigating the role of radiation-induced damage-associated molecular patterns (DAMPs) in cancer[32] and ways to manipulate these immune responses in specific organs such as the liver.[33] In order to properly characterize these responses, it is necessary to deliver a conformal radiation dose to the liver while sparing the surrounding normal tissue and other organs. To simulate such an experiment, a mouse CT scan was acquired using contrast for better delineation of the liver and kidneys. Contours were drawn for these two structures and transferred to analogous positions on the body contour of the mouse phantom CT. The planning objective was to deliver a dose of 10 Gy to the whole liver while sparing the dose to the kidneys and surrounding normal tissue.

The third experiment was designed to evaluate the level of 2D dose complexity achievable with the SOC and create a plan well-suited for evaluating the commissioning steps described in the following section. For this plan, an image of Audrey Hepburn was downsampled and simplified to three dose prescription levels of 2, 4, and 6 Gy. This target dose pattern lends itself to a wide range of aperture sizes, making it ideal for evaluating field size-specific effects on the dose distribution.

For each of the mouse plans, the dose was calculated for 180 coplanar beams with 2° separation using a convolution/superposition algorithm with a 225 kV polyenergetic kernel tuned to match the PDD of the SmART system for a 2.5 cm (Mouse U and UC) or 1 mm (Mouse Liver and Audrey) field size. The justification and measurement of this 1 mm field size energy spectrum is detailed in a later section. The voxel resolution was 0.5 mm^3 for the Mouse U and UC plans and 0.1 mm^3 for the Mouse Liver and Audrey plans. The 4π beam orientation optimization method, which differs from the RAO method described and has

been previously published extensively,[34–44] was then used to find optimal beam angles for each plan. This optimization is based on a greedy column generation approach which iteratively selects beams from a candidate pool. Since the Mouse U and UC plans aimed to evaluate the highest achievable SOC plan quality, 20 optimal beams were selected and a beamlet size (and minimum aperture size) of 0.5 mm^2 was used. The Mouse Liver case was planned more conservatively, with a more realistically deliverable beam count of 5 and a minimum aperture size of 1 mm^2. The Audrey plan was also optimized for a 1 mm^2 beamlet size. RAO was then applied for each plan, with a shell structure added around the PTV for the mouse plans to minimize dose spillage. The mouse plan doses were scaled to deliver the prescription dose to 95% of the target volume. Since these target volumes were created for demonstration purposes, there were no specific margins added. The dimensions of such treatment margins in real mice would depend on the overall geometric and setup uncertainty of the system (discussed in Part II of this report), as well as the type of disease, including the risk of microscopic extension and potential motion uncertainties.

As dosimetric endpoints for evaluation, R_{50} and PTV homogeneity $\left(\frac{D95}{D5}\right)$ were assessed. R_{50} is a measure of high dose spillage, defined as the ratio between the 50% isodose volume and the PTV volume. The van't Riet conformation number (CN) was also assessed.[45] CN is defined as $CN = \frac{TV_{RI}}{TV} \times \frac{TV_{RI}}{V_{RI}}$, where TV_{RI} is the target volume covered by the prescription dose, TV is the target volume, and V_{RI} is the volume of the prescription dose.

Beam Commissioning Measurements

The optimization method described above assumes the same output, energy spectrum, and penumbra for all aperture sizes and locations, and does not account for any system-specific characteristics or imperfections. Therefore, a series of beam commissioning measurements, detailed in Table 1, were performed on our X-RAD SmART system in order to improve the dosimetric accuracy of RAO IMRT plans delivered on this system. All measurements were done at an energy of 225 kV and source surface distance (SSD) of 30.5 cm with 0.32 mm added copper filtration. Film measurements were performed with Gafchromic EBT3 film (lot #10161801) (Ashland Inc., Covington, KY), oriented perpendicular to the beam on the surface of a solid water phantom, and scanned on an Epson 10000XL scanner with a resolution of 96 dpi in 48-bit RGB (red, green, and blue). Film doses were analyzed with Ashland's FilmQA Pro software using a red channel calibration curve created from the same film lot according to the manufacturer-recommended protocol.[46] Calibration film irradiations were performed on the surface of solid water and absolute doses were determined using the AAPM Task Group 61 protocol for in-air dose calibration of low- and medium-energy x-rays.[47] The 40 × 40 mm square stationary collimator for the SmART system was used for the larger field measurements. All field sizes <40 mm were created using a prototype SOC system. Briefly, the SOC design consists of four pairs of orthogonal, double-focused tungsten leaves driven by Arduino-controlled stepper motors with rotary encoders for leaf position verification. The SOC system is mounted onto the 40 × 40 mm collimator of the SmART. The complete design, fabrication, installation, and commissioning of the SOC is detailed in Part II of this report.

Off-axis factors were determined by delivering an array of fields (5, 2.5, or 1 mm square) spaced 1.5 mm apart over the full SOC field to a single film. The mean dose in the center of each field was measured, and an interpolation was performed over the full field. An off-axis factor was then defined at each point in the field by the ratio of this dose to the central axis dose. Preliminary measurements showed no significant difference in off axis output for fields >5 mm.

Percent depth dose was measured with film stacked between slabs of solid water perpendicular to the beam at intervals of 2 mm (0 to 15 mm depth), 5 mm (15 to 60 mm depth) and 10 mm (60 to 90 mm depth). The measured PDD data was used to generate an estimated energy spectrum for each field size, with mean and maximum allowed PDD deviations of <2% and <5%, respectively. These spectra were obtained by first using the dose calculation method previously described with a virtual water phantom to generate 40 different PDD curves (spanning the range of the measured curves) for beams with slightly different attenuation properties. The convex optimization software CVX (CVX Research, Inc., Austin, TX) was then used to find the optimal weighting of each curve to best match the measured PDD.

Plan Post-Processing

This data was then integrated into the treatment planning process. Originally, the dose was calculated using a single general energy spectrum, previously tuned for a 20 × 20 mm field on the SmART, and the plan was optimized using this dose matrix. However, this optimized plan may include a wide range of aperture sizes, and the calculated dose will theoretically only be accurate for 20 × 20 mm apertures.

Therefore, instead of performing the initial dose calculation with a single energy spectrum, this step was updated to calculate five different dose distributions using the estimated energy spectra for 1, 3, 5, 10, and 20 mm field sizes. After optimization, the final apertures can then be separated by closest equivalent square field size, multiplied by the appropriate dose matrix and optimized weighting value (a), and summed together to get a potentially more accurate, aperture size specific dose distribution. Since the plan quality is typically degraded to some extent after dose recalculation, the aperture weightings are then re-optimized to match the original optimized dose as closely as possible.

Since five different initial dose matrices are calculated now, the remaining question is which should be used for the initial optimization. This was explored by performing the rectangular aperture optimization for the same plan using the dose calculated for each of the five energy spectra. The difference between each optimized dose and the recalculated field size-specific dose was then analyzed. The Audrey plan was ideal for this analysis because of its wide range of aperture sizes (a preliminary optimization selected apertures ranging from 1 to 20 mm equivalent squares).

The weighting for each aperture is then converted to a dwell time based on the measured absolute output and scaled by output factor using the equivalent square field size. In addition to output factor scaling, apertures ≤5 mm are matched by equivalent square size to the closest off-axis factor map and scaled according to their location within the SOC field.

Once the final apertures and dwell times have been calculated, the plan is prepared for delivery with the SOC hardware, described in the following section. The basic SOC design enables apertures in diagonal quadrants to be delivered simultaneously, greatly improving the plan delivery efficiency. Therefore the apertures are then categorized by quadrant, and apertures in diagonal quadrants are combined to be delivered in parallel. The apertures are also sorted by dwell time prior to combination so that the longest times are paired together, further increasing delivery efficiency.

Results

RAO Plan Analysis

In the first experiment, the average number of deliverable apertures per beam was 11.5 and 10.5 for the Mouse U and UC cases, respectively. Figure 1 shows the resulting dose distributions for highly concave RAO IMRT plans inside the mouse brain. Both hypothetical MLC and SOC plans achieved conformal dose distributions, but the SOC plans had higher homogeneity within the target volume. The poorer performance of the MLC is due in part to the extra segmentation step from the fluence map to deliverable apertures, which is avoided with the DAO method used for the SOC plans. The SOC was also able to create the more complex UC target while sparing the normal brain. The PTV homogeneity, R_{50}, and CN for the Mouse U and UC cases are given in Table 2. For the Mouse U case, the SOC plans were superior to the MLC plans in all categories. The Mouse UC SOC plan achieved acceptable conformity and homogeneity while minimizing the high dose spillage.

In the second experiment, RAO achieved a highly conformal dose to the mouse liver while sparing the dose to the kidneys, as shown in the DVH and dose wash in Figure 2, demonstrating a realistic application for the SOC. The plan achieved relatively high target homogeneity and conformity with low dose spillage, as demonstrated by the evaluation metrics given in Table 2. Most importantly, this high quality dose distribution was achieved using realistic delivery parameters of five beams and 1 × 1 mm minimum aperture size.

The resulting dose distribution for the Audrey RAO IMRT plan is shown in Figure 3. This complex target image, with four dose levels (including 0 Gy) and 1 mm resolution, was closely replicated with RAO using a total of 551 apertures with a mean size of 2.4 × 2.4 mm. Due to the high number of small fields, this corresponds to an estimated delivery time of approximately 18 minutes (after applying the output and off-axis factors presented in the following section). While this would be impractically high for a single beam of a mouse SOC plan, it is certainly feasible for delivery as a proof-of-concept.

Beam Commissioning

The absolute output of the SmART was 0.461 cGy/mAs, and the measured output factors are shown in Figure 4. A logarithmic curve was fit to the average measurements for field sizes 2.5 to 25 mm with an R^2 value of 0.9916. Since the output dropped significantly for 1 mm fields and a simple curve could not closely fit all data points, a separate logarithmic equation was used for fields 1 to 2.5 mm. These relationships are used to scale each aperture by output factor based on its equivalent square field size. The smallest field size for which the

output could be reliably measured with film was 1 mm, for which the output factor was 0.747 ± 0.025. Therefore, although the orthogonal SOC design is theoretically capable of achieving smaller aperture sizes, and the goal of the system is to eventually achieve submillimeter accuracy and precision, for now the minimum beamlet size for SOC-based IMRT is limited to 1 mm. This inconsistency in submillimeter field dosimetry is likely the result of slight leaf positioning errors, which have a large effect on small field sizes due to occlusion of the ~3 mm diameter focal spot. There may also be error resulting from an inhomogeneous focal spot distribution, which has been observed in previous studies[48] and will be discussed in a later section.

Simplified off-axis factor data for field sizes 5, 2.5, and 1 mm is given in Table 3 for comparative purposes, with the measurement and calculation process illustrated in Figure 5 for 2.5 mm fields. The highest output was measured in the center of the SOC field for all three field sizes and was therefore the reference point for all other region measurements. The minimum off-axis factors were 0.956, 0.910, and 0.650 for field sizes 5, 2.5, and 1 mm, respectively. The minimum and maximum (excluding the center) output factors were measured in the same SOC field regions for the 2.5 and 1 mm fields, but differed for the 5 mm field, although the effect is minimal for this larger field size. The full interpolated maps, such as the one shown in Figure 5, right, are used for the final off-axis aperture scaling.

The PDD measurements for square field sizes 1 to 40 mm are plotted in Figure 6, along with the matched energy spectra curves. Each spectrum is a weighted combination of two to three of the 40 candidate beams. The average maximum and mean differences between the measured and matched PDD curves were 4.47 ± 0.30% and 1.71 ± 0.18%, respectively. For depths of 1 to 2 cm and field sizes ≤1 cm, which would be the most relevant for small animal experiments, the average maximum difference from the measured PDD data is only 3.3%.

Dose Recalculation

For the Audrey plan dose recalculation assessment, the five plans optimized with each dose matrix (calculated for energy spectra tuned to 1, 3, 5, 10, and 20 mm field sizes) all selected at least two apertures of each closest equivalent square field size. The most common aperture size selected for each plan was 1 mm (66.8 ± 1.0%). This decreased with increasing field size, with a least common aperture size of 20 mm (0.6 ± 0.1%). The difference between the optimized and recalculated dose for each plan is shown in Figure 7 (upper), and the mean and maximum dose deviations, as well as the complete aperture size breakdown, are given in Table 4.

The spatial distribution of the dose deviations is intuitive, with most of the error arising from the largest apertures in the 1 mm optimization and from the smallest apertures in the 20 mm optimization, while the 5 mm optimization shows a mix of both. The 1 mm optimized plan had a mean dose deviation of only 1.2% of the maximum dose, compared to ≥3% for the other plans, likely because the majority of apertures were closest to this field size. The 10 and 20 mm optimized plans had the lowest maximum dose deviation of 9.7%, despite these field sizes making up only ~2.2% and ~0.6% of the total apertures, respectively. The 5 mm optimized plan had the highest mean deviation (3.4%) and the 3 mm plan had the highest maximum deviation (16.0%), which suggests that “compromising” with one of the middle

aperture sizes may not be a good strategy. The optimization process is currently being updated to enable the dose to be optimized directly with the correct dose distribution for each aperture size. This will eliminate the need for any dose recalculation or reoptimization, reducing the overall treatment planning time and potentially resulting in higher quality RAO plans.

For the same test plan, the maximum difference between the original optimized dose (for 1 mm field size) and the recalculated dose was reduced from 11.0% to 7.3% of the maximum dose after reoptimization of the aperture weightings. The mean difference was maintained at 1.2%. These differences in dose distribution are shown in Figure 7 (lower).

Discussion

The gap between human radiotherapy and preclinical animal studies has widened with the utilization of IMRT and other more sophisticated techniques, including 4π radiotherapy. This increasing discrepancy in dose conformality can adversely impact the ability to translate animal studies to effective human trials. Due to a difference in size of one to two orders of magnitude, direct translation of the MLC used in human radiotherapy has met insurmountable engineering difficulties. In this study, we described an alternative approach using a sparse orthogonal collimator for small animal IMRT. With the RAO SOC test cases, we demonstrated the ability to create highly conformal plans with concave and complex targets.

It is evident from our beam commissioning measurements that the accurate characterization of small, off-axis fields is currently the limiting factor in terms of the minimum SOC aperture size. However, some of the main sources of error with these measurements are due to fundamental limitations of the SmART system itself and the temporary gantry mounting of the prototype SOC (described in Part II of this report), rather than the SOC design. Despite our best effort, there are some challenges mounting the SOC onto the SmART system gantry, causing slight misalignment with each installation. Even with leaf position re-calibration, the misalignment can introduce detectable residual error for fields smaller than the 3 mm diameter focal spot. While the SmART system does have a smaller focal spot option, the low output would lead to prohibitively long treatment times.

Even with perfect SOC alignment, the dosimetry of submillimeter field sizes would likely still be a challenge. Tryggestad et al performed a pinhole experiment with a similar source (225 kVp, 3 mm large focal spot) on the SARRP and found that the focal spot had a highly inhomogeneous intensity, significantly affecting the dose distribution from a 0.5 mm aperture[48]. These effects were much less significant for 1 mm fields, resulting in only slight asymmetry. In order to reduce the minimum SOC aperture size below 1 mm, we would need to fully characterize the large focal spot fluence distribution and incorporate this into our dose calculation engine for more accurate small field dose predictions.

Despite these uncertainties, the SOC is better suited for small animal radiotherapy than the MLC. In addition to the simplified hardware design, the SOC has advantages in terms of the optimization algorithm. While the MLC can conform to more arbitrary shapes, the SOC is

seemingly limited in the complexity of its apertures. However, this limitation is advantageous in solving the direct aperture optimization problem using the rectangular basis, since the dose degradation during the fluence map to MLC aperture conversion is avoided. This results in high quality plans and in some cases, such as the U target plan, more homogeneous and conformal PTV doses. Our analytical rectangular direct aperture optimization method is distinctly different from previous “jaws-only” optimization approaches[49,50] using a stochastic simulated annealing method, which is slow and cannot search all available apertures.

Also, unlike with human treatments, trained dosimetrists and medical physicists are unaffordable in preclinical studies. Therefore, any small animal treatment planning system must be fast and highly automated in order to be a realistic and desirable alternative to current methods. The current optimization time is approximately 30 seconds for a typical 7 beam IMRT plan, enabling short planning times and high throughput. Although the target and avoidance structures would still need to be specified, automated contouring methods could potentially be employed, and the rest of the proposed planning system requires very limited user input. With the use of automated beam selection, followed by rectangular aperture optimization and system-specific plan post-processing, high quality treatment plans can be created for SOC delivery without any special training or lengthy planning processes.

Conclusions

By using advanced optimization techniques, complex IMRT plans were achieved using a simple dose modulation device: sparse orthogonal collimator. Beam commissioning data was incorporated into the treatment planning process to more accurately predict the resulting dose distribution. This novel IMRT platform substantially reduces the gap in treatment plan quality between clinical and preclinical radiotherapy, potentially increasing the translatability of small animal studies.

Acknowledgements

This research was supported by NIH grants R21CA228160 and U19AI067769.

References

1. Delaney G, Jacob S, Featherstone C, Barton M. The role of radiotherapy in cancer treatment: estimating optimal utilization from a review of evidence-based clinical guidelines. Cancer. 2005;104(6):1129–1137. [PubMed: 16080176]
2. Barton MB, Jacob S, Shafiq J, et al. Estimating the demand for radiotherapy from the evidence: a review of changes from 2003 to 2012. Radiotherapy and oncology : journal of the European Society for Therapeutic Radiology and Oncology. 2014;112(1):140–144. [PubMed: 24833561]
3. Coleman CN, Higgins GS, Brown JM, et al. Improving the Predictive Value of Preclinical Studies in Support of Radiotherapy Clinical Trials. Clinical cancer research : an official journal of the American Association for Cancer Research. 2016;22(13):3138–3147. [PubMed: 27154913]
4. Harrington KJ, Billingham LJ, Brunner TB, et al. Guidelines for preclinical and early phase clinical assessment of novel radiosensitisers2011;No. 5:628–639. Located at: Br J Cancer.
5. Kahn J, Tofilon PJ, Camphausen K. Preclinical models in radiation oncology. Radiation Oncology. 2012;7(1):223. [PubMed: 23270380]

6. Rosenthal N, Brown S. The mouse ascending: perspectives for human-disease models. Nature cell biology. 2007;9(9):993–999. [PubMed: 17762889]
7. Van Dyke T, Jacks T. Cancer modeling in the modern era: progress and challenges. Cell. 2002;108(2):135–144. [PubMed: 11832204]
8. Mak IW, Evaniew N, Ghert M. Lost in translation: animal models and clinical trials in cancer treatment. American journal of translational research. 2014;6(2):114–118. [PubMed: 24489990]
9. Denayer T, Stöhr T, Van Roy M. Animal models in translational medicine: Validation and prediction. New Horizons in Translational Medicine. 2014;2(1):5–11.
10. Day C-P, Merlino G, Van Dyke T. Preclinical Mouse Cancer Models: A Maze of Opportunities and Challenges. Cell. 2015;163(1):39–53. [PubMed: 26406370]
11. Hackam DG, Redelmeier DA. Translation of research evidence from animals to humans. Jama. 2006;296(14):1731–1732. [PubMed: 17032985]
12. Liu FF, Okunieff P, Bernhard EJ, et al. Lessons learned from radiation oncology clinical trials. Clinical cancer research : an official journal of the American Association for Cancer Research. 2013;19(22):6089–6100. [PubMed: 24043463]
13. Stuben G, Landuyt W, van der Schueren E, van der Kogel AJ. Different immobilization procedures during irradiation influence the estimation of alpha/beta ratios in mouse lip mucosa. Strahlentherapie und Onkologie : Organ der Deutschen Rontgengesellschaft [et al.]. 1993;169(11): 678–683.
14. Kitakabu Y, Shibamoto Y, Sasai K, Ono K, Abe M. Variations of the hypoxic fraction in the SCC VII tumors after single dose and during fractionated radiation therapy: assessment without anesthesia or physical restraint of mice. International journal of radiation oncology, biology, physics. 1991;20(4):709–714.
15. Nikjoo H, Lindborg L. RBE of low energy electrons and photons. Physics in medicine and biology. 2010;55(10):R65–109. [PubMed: 20427859]
16. Chow JC, Leung MK, Lindsay PE, Jaffray DA. Dosimetric variation due to the photon beam energy in the small-animal irradiation: a Monte Carlo study. Medical Physics. 2010;37(10):5322–5329. [PubMed: 21089767]
17. Verhaegen F, van Hoof S, Granton PV, Trani D. A review of treatment planning for precision image-guided photon beam pre-clinical animal radiation studies. Zeitschrift fur medizinische Physik. 2014;24(4):323–334. [PubMed: 24629309]
18. Granton PV, Verhaegen F. On the use of an analytic source model for dose calculations in precision image-guided small animal radiotherapy. Physics in medicine and biology. 2013;58(10):3377–3395. [PubMed: 23615380]
19. Desrosiers M, DeWerd L, Deye J, et al. The Importance of Dosimetry Standardization in Radiobiology. J Res Natl Inst Stand Technol. 2013;118:403–418. [PubMed: 26401441]
20. Yoshizumi T, Brady SL, Robbins ME, Bourland JD. Specific issues in small animal dosimetry and irradiator calibration. International journal of radiation biology. 2011;87(10):1001–1010. [PubMed: 21961967]
21. Butterworth KT, Prise KM, Verhaegen F. Small animal image-guided radiotherapy: status, considerations and potential for translational impact. Br J Radiol. 2015;88(1045).
22. Wong J, Armour E, Kazanzides P, et al. High-resolution, small animal radiation research platform with x-ray tomographic guidance capabilities. International journal of radiation oncology, biology, physics. 2008;71(5):1591–1599.
23. Pidikiti R, Stojadinovic S, Speiser M, et al. Dosimetric characterization of an image-guided stereotactic small animal irradiator. Physics in medicine and biology. 2011;56(8):2585–2599. [PubMed: 21444969]
24. Stewart JM, Lindsay PE, Jaffray DA. Two-dimensional inverse planning and delivery with a preclinical image guided microirradiator. Medical Physics. 2013;40(10):101709. [PubMed: 24089899]
25. Reinhart AM, Nill S, Oelfke U. μIMRT on the SARRP using the motorised variable collimator Paper presented at: Fourth International Conference on Precision Image-Guided Small Animal Radiotherapy Research2018; Lisbon, Portugal.

26. Nguyen D, Ruan D, O'Connor D, et al. A novel software and conceptual design of the hardware platform for intensity modulated radiation therapy. Medical Physics. 2016;43(2):917–929. [PubMed: 26843252]
27. Chambolle A, Pock T. A First-Order Primal-Dual Algorithm for Convex Problems withApplications to Imaging. Journal of Mathematical Imaging and Vision. 2011;40(1):120–145.
28. Pock T, Chambolle A. Diagonal preconditioning for first order primal-dual algorithms in convex optimization. Paper presented at: Computer Vision (ICCV), 2011 IEEE International Conference on2011.
29. Pock T, Cremers D, Bischof H, Chambolle A. An algorithm for minimizing the Mumford-Shah functional. Paper presented at: Computer Vision, 2009 IEEE 12th International Conference on2009.
30. Condat L A Primal–Dual Splitting Method for Convex Optimization Involving Lipschitzian, Proximable and Linear Composite Terms. Journal of Optimization Theory and Applications. 2013;158(2):460–479.
31. Nguyen D, O'Connor D, Yu VY, et al. Dose domain regularization of MLC leaf patterns for highly complex IMRT plans. Medical Physics. 2015;42(4):1858–1870. [PubMed: 25832076]
32. Schaue D, McBride WH. Links between Innate Immunity and Normal Tissue Radiobiology. Radiat Res. 2010;173(4):406–417. [PubMed: 20334512]
33. Huang XW, Yang J, Dragovic AF, Zhang H, Lawrence TS, Zhang M. Antisense oligonucleotide inhibition of tumor necrosis factor receptor 1 protects the liver from radiation-induced apoptosis. Clinical cancer research : an official journal of the American Association for Cancer Research. 2006;12(9):2849–2855. [PubMed: 16675580]
34. Dong P, Lee P, Ruan D, et al. 4π non-coplanar liver SBRT: a novel delivery technique. International journal of radiation oncology, biology, physics. 2013;85.
35. Dong P, Lee P, Ruan D, et al. 4pi noncoplanar stereotactic body radiation therapy for centrally located or larger lung tumors. International journal of radiation oncology, biology, physics. 2013;86(3):407–413.
36. Rwigema JC, Nguyen D, Heron DE, et al. 4pi noncoplanar stereotactic body radiation therapy for head-and-neck cancer: potential to improve tumor control and late toxicity. International journal of radiation oncology, biology, physics. 2015;91(2):401–409.
37. Tran A, Zhang J, Woods K, et al. Treatment planning comparison of IMPT, VMAT and 4π radiotherapy for prostate cases. Radiation Oncology. 2017;12(1):10. [PubMed: 28077128]
38. Nguyen D, Rwigema JC, Yu VY, et al. Feasibility of extreme dose escalation for glioblastoma multiforme using 4π radiotherapy. Radiation oncology (London, England). 2014;9.
39. Yu VY, Tran A, Nguyen D, et al. Significant Cord and Esophagus Dose Reduction by 4π Non-Coplanar Spine Stereotactic Body Radiation Therapy and Stereotactic Radiosurgery. International journal of radiation oncology, biology, physics. 2016;96(2).
40. Yu VY, Landers A, Woods K, et al. A Prospective 4π Radiotherapy Clinical Study in Recurrent High Grade Glioma Patients. International journal of radiation oncology, biology, physics. 2018;101(1):144–151.
41. Yu VY, Tran A, Nguyen D, et al. The development and verification of a highly accurate collision prediction model for automated noncoplanar plan delivery. Medical Physics. 2015;42(11):6457–6467. [PubMed: 26520735]
42. Woods K, Nguyen D, Tran A, et al. Viability of Non-Coplanar VMAT for Liver SBRT as Compared to Coplanar VMAT and Beam Orientation Optimized 4pi IMRT. Advances in radiation oncology. 2016;1(1):67–75. [PubMed: 27104216]
43. Woods K, Lee P, Kaprealian T, Yang I, Sheng K. Cochlea-sparing acoustic neuroma treatment with 4π radiotherapy. Advances in radiation oncology. 2018;3(2):100–107. [PubMed: 29904732]
44. Murzin VL, Woods K, Moiseenko V, et al. 4π plan optimization for cortical-sparing brain radiotherapy. Radiotherapy and Oncology. 2018;In Press.
45. Van't Riet A, Mak AC, Moerland MA, Elders LH, van der Zee W. A conformation number to quantify the degree of conformality in brachytherapy and external beam irradiation: application to the prostate. International Journal of Radiation Oncology* Biology* Physics. 1997;37(3):731–736.
46. Ashland Inc. Efficient Protocols for Calibration and Dosimetry. 2016.

47. Ma CM, Coffey CW, DeWerd LA, et al. AAPM protocol for 40–300 kV x-ray beam dosimetry in radiotherapy and radiobiology. Medical Physics. 2001;28(6):868–893. [PubMed: 11439485]

48. Tryggestad E, Armour M, Iordachita I, Verhaegen F, Wong JW. A comprehensive system for dosimetric commissioning and Monte Carlo validation for the small animal radiation research platform. Physics in medicine and biology. 2009;54(17):5341–5357. [PubMed: 19687532]

49. Earl MA, Afghan MK, Yu CX, Jiang Z, Shepard DM. Jaws-only IMRT using direct aperture optimization. Medical Physics. 2007;34(1):307–314. [PubMed: 17278516]

50. Kim Y, Verhey LJ, Xia P. A feasibility study of using conventional jaws to deliver IMRT plans in the treatment of prostate cancer. Physics in medicine and biology. 2007;52(8):2147–2156. [PubMed: 17404460]

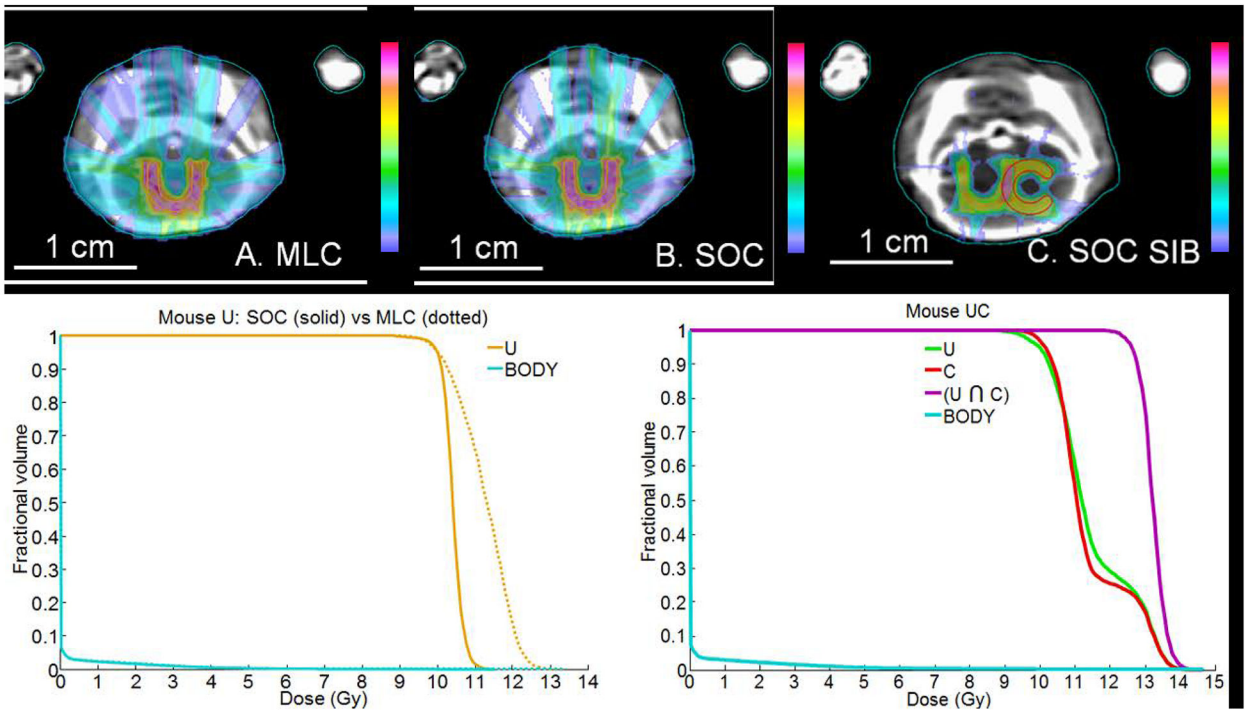

Figure 1.

(Upper) Calculated concave dose distribution (with colorbar units in Gy) in the mouse brain delivered with a hypothetical MLC (A) and the SOC (B). Simultaneous integrated boost SOC plan (C) with a 125% dose boost to the overlapping target region. (Lower) Dose volume histogram comparisons for plans in (A-C). The SOC plans show a more homogeneous dose with less high dose spillage using the same number of segments.

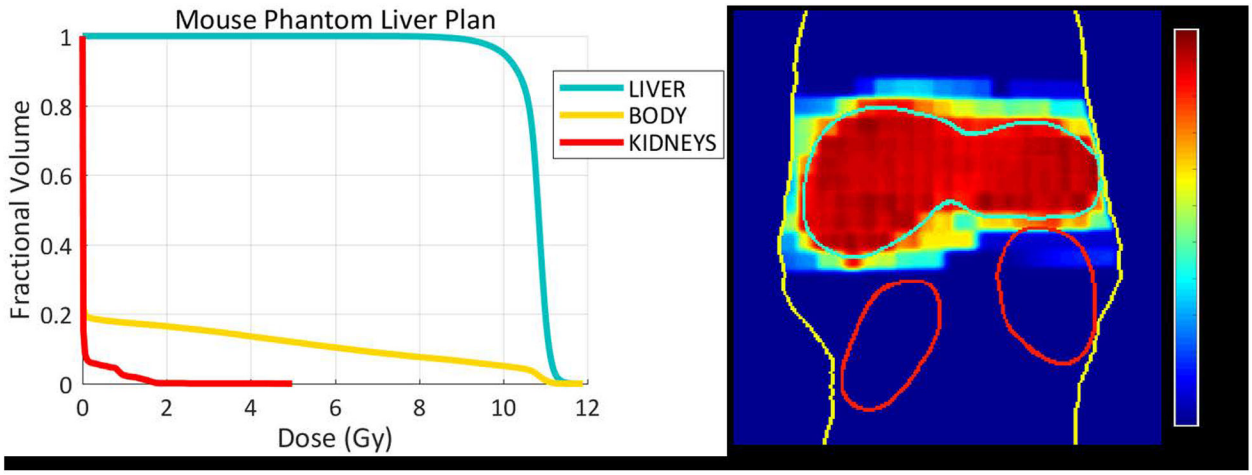

Figure 2.

Dose volume histograms (left) and dose wash (right) for the mouse phantom whole liver irradiation plan, optimized with RAO. In both images, the liver (target) is shown in teal, body in yellow, and kidneys in red.

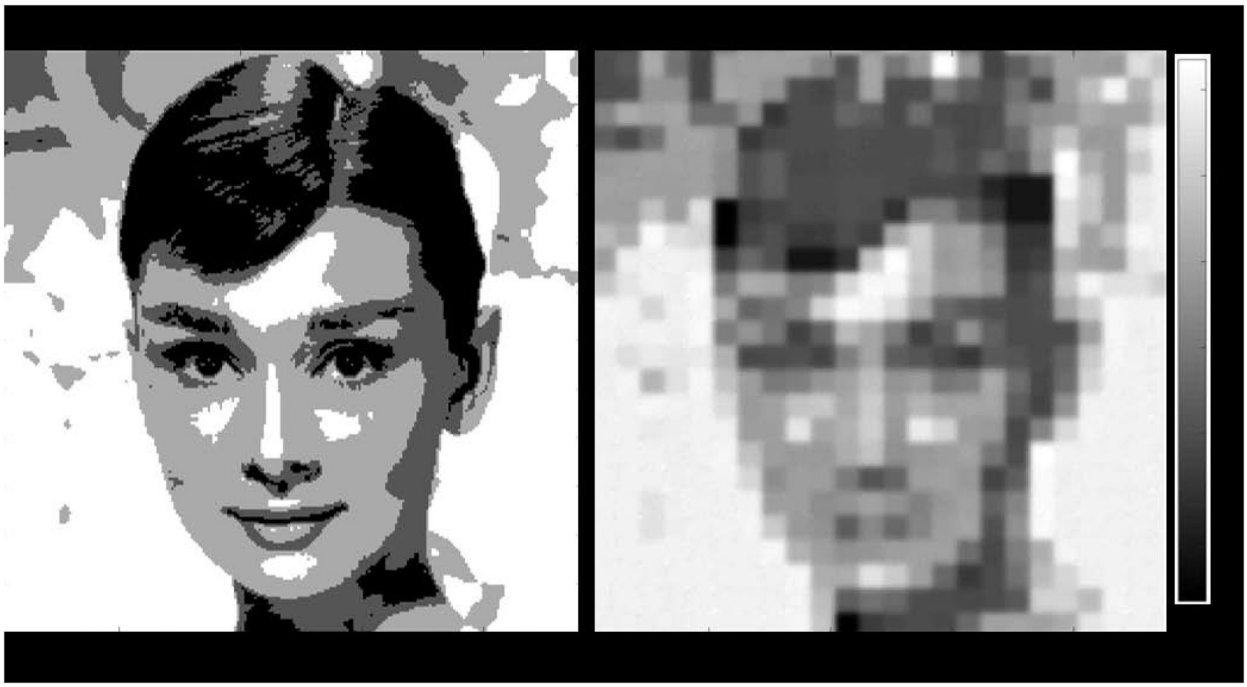

Figure 3.
(Left) Target image for the Audrey Hepburn plan, with four dose levels of 0, 2, 4, and 6 Gy. (Right) Optimized dose distribution from RAO with 1 mm beamlet and minimum aperture size. The optimized plan used 551 apertures with an average size of 2.4 mm.

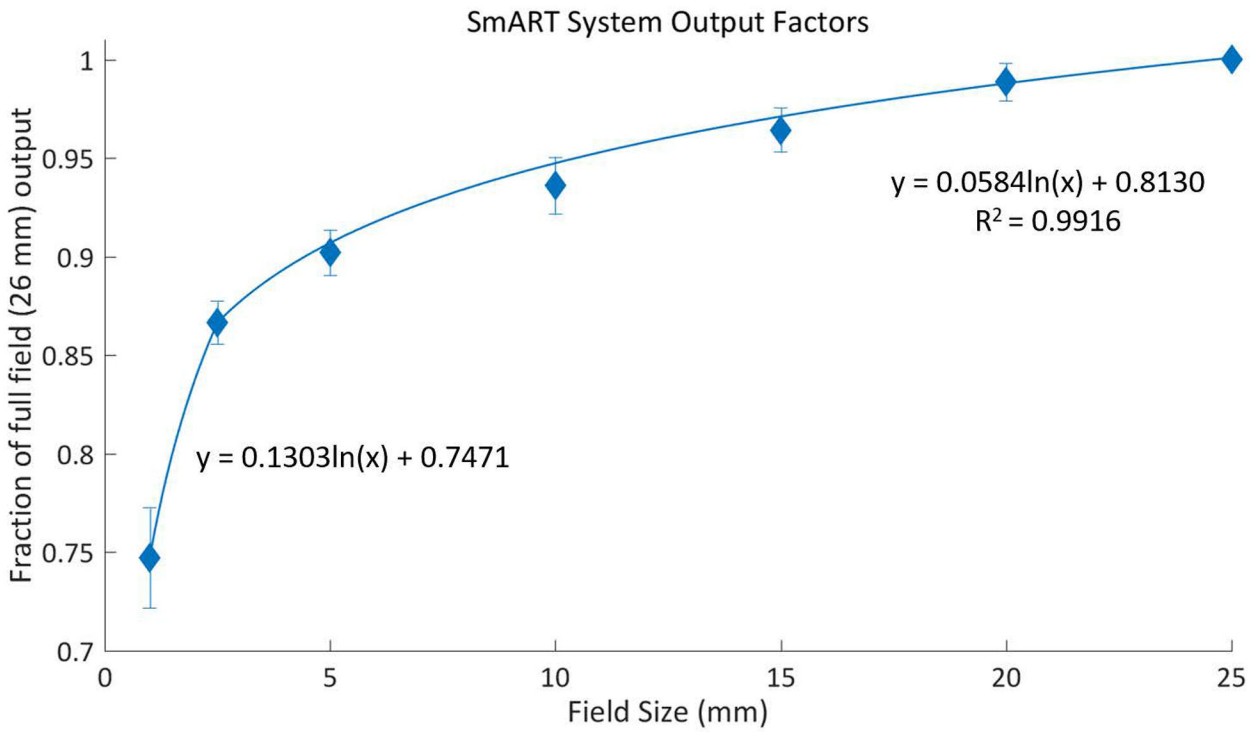

Figure 4.

Measured output factors (average and standard deviation shown for four measurements) for the SmART system, calculated as a fraction of the full 26 mm SOC field.

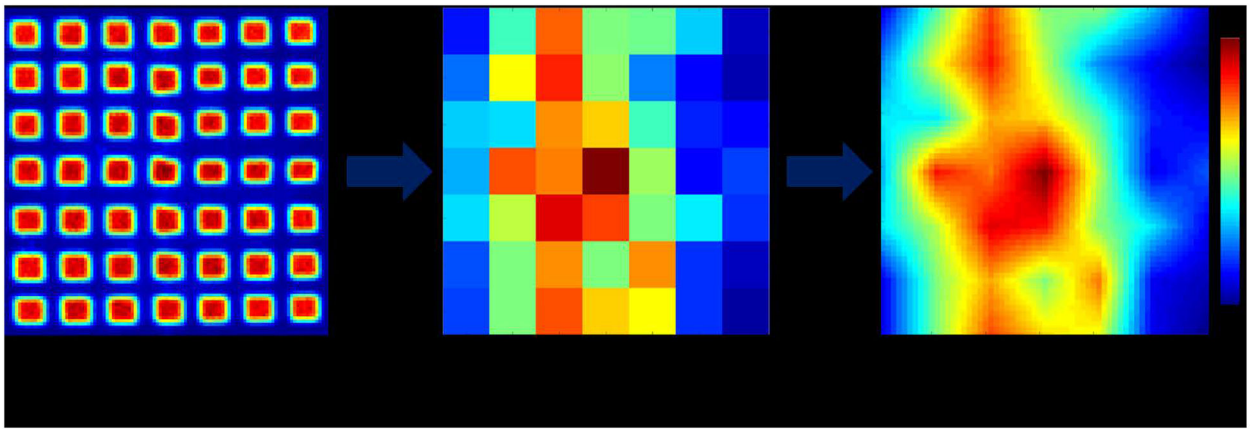

Figure 5.

The off-axis factor calculation process for 2.5 mm field sizes. (A) The measured film dose distribution for an array of 2.5 mm fields, normalized to 1; (B) the measured mean central dose values for each field in A; (C) the dose values in B interpolated over the full SOC field.

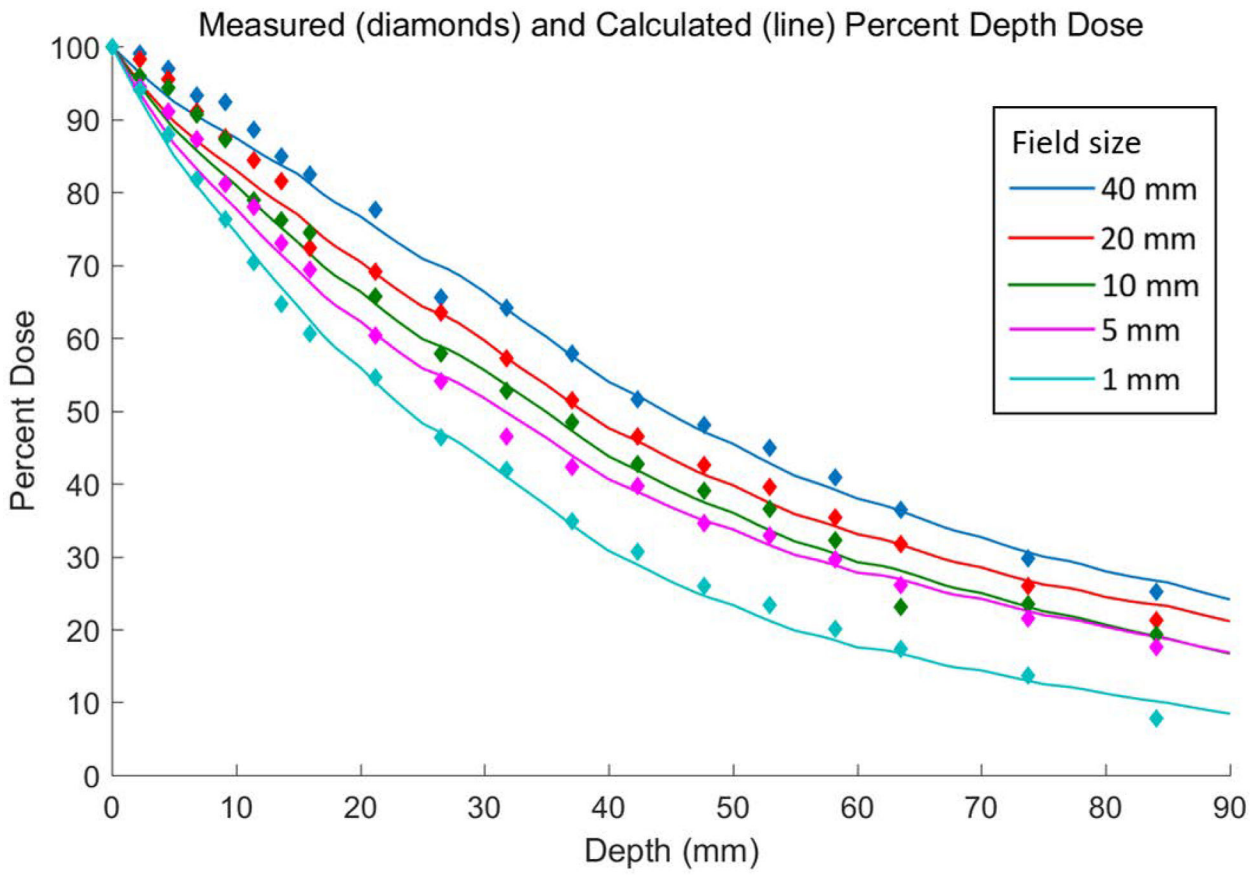

Figure 6.

Percent depth dose data for different field sizes measured on the SmART (diamonds) and for the energy spectra optimized to match the measured data (lines).

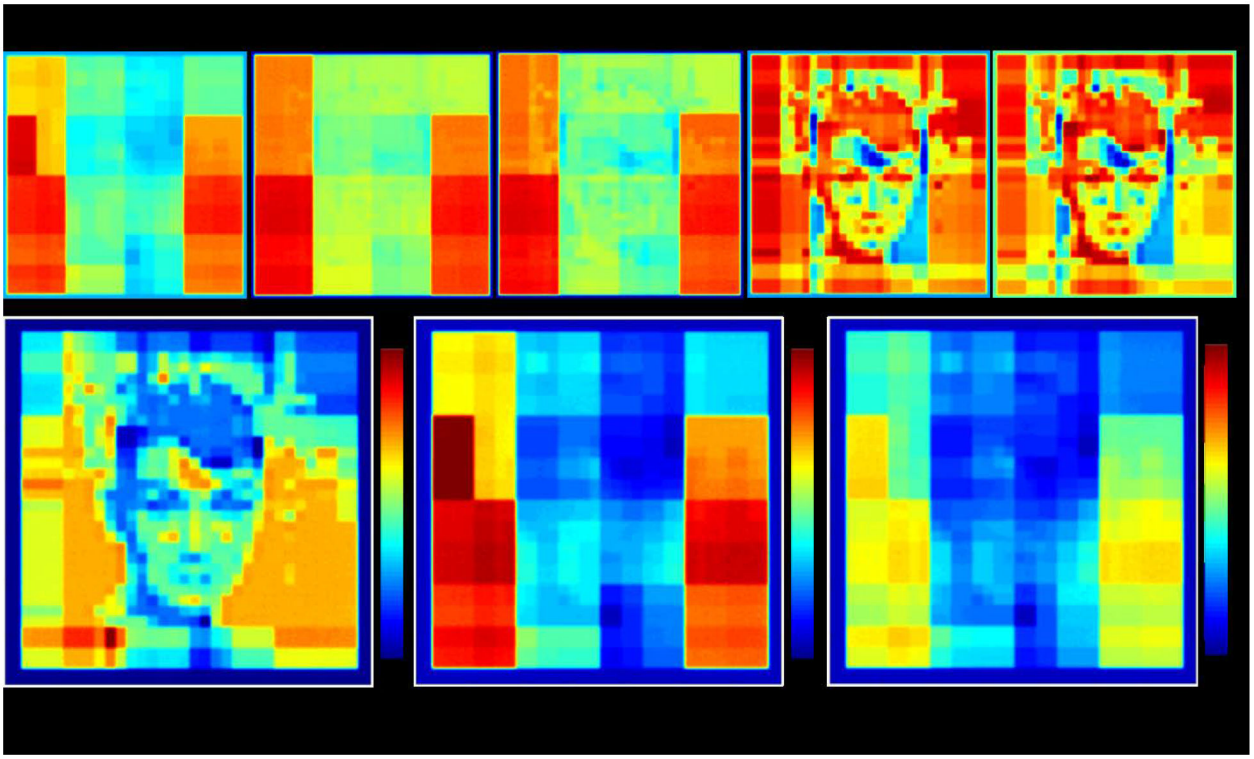

Figure 7.

(Upper) Difference from the recalculated (field size-specific) dose for each optimization spectrum. (Lower) Dose optimized with the 1 mm field calculation spectrum (left), difference between the optimized dose and the recalculated dose, with a mean of 1.2% and maximum of 11.0% of the maximum plan dose (middle), difference between the optimized dose and the dose after reoptimization of the aperture weightings, with a mean of 1.2% and a maximum of 7.3% of the maximum plan dose (right). (D_{opt}: original optimized dose; D_{recalc}: optimized dose recalculated based on aperture size; D_{reopt}: dose after reoptimization of aperture weightings)

Table 1.

SmART system beam commissioning measurement parameters

Measurement	Equipment	Square field sizes (mm)	Depth	Calculation details
Absolute output	Ionization chamber, electrometer	40	In air	AAPM Task Group 61 protocol[47] (average of 3 measurements)
Output factor	EBT3 film, solid water sheets	26, 20, 15, 10, 5, 2.5, 1	2 mm	$\frac{mean\ dose(field\ size\ x)}{mean\ dose\ (26\ mm\ field)}$ (average of 4 measurements)
Off-axis factors		5, 2.5, 1 (1.5 mm apart over entire SOC field)	2 mm	$\frac{mean\ dose(\ location\ x)}{mean\ dose\ (center)}$
Percent depth dose		40, 20, 10, 5, 1	Down to 10 cm	$\frac{mean\ dose(\ depth\ x)}{max(all\ mean\ depth\ doses)}$

Table 2.

Dose evaluation metrics for the mouse test cases (R_{50}: 50% dose spillage; CN: van't Riet Conformation Number)

Plan	Target	Homogeneity	R_{50}	CN
Mouse U (SOC)	U	0.922	4.459	0.753
Mouse U (MLC)	U	0.815	4.818	0.626
Mouse UC (SOC)	U - C	0.888	3.862	0.713
	C - U	0.896		
	U ∩ C	0.914	N/A[a]	0.711
Mouse Liver (SOC)	Liver	0.895	2.204	0.856

[a] No R_{50} calculation for the U ∩ C volume was made since the dose to the non-overlapping volume would be included in the calculation.

Table 3.

Simplified off-axis factor measurements for 1, 2.5, and 5 mm square SOC fields on the SmART system, averaged over nine equal regions for comparison

Off-Axis Factors (shown according to SOC field location)								
1 mm			2.5 mm			5 mm		
.70	.70	.65[b]	.94	.96	.91[b]	.97	.99	.99
.75	1.00	.70	.96	1.00	.93	.98	1.00	1.00[a]
.70	.80[a]	.65[b]	.93	.97[a]	.91[b]	.96[b]	.97	.97

[a]Maximum off-axis factor (excluding the center region)

[b]Minimum off-axis factor

Table 4.

Error comparison for plans optimized with different dose calculation spectra

Optimization Dose Matrix (energy spectrum field size, mm)	Optimized Dose – Recalculated Dose (absolute voxelwise comparison, % of maximum dose)	
	Mean	*Maximum*
1	1.2	11.0
3	3.0	16.0
5	3.4	14.7
10	3.1	9.7
20	3.2	9.7